Journal of
Materials Chemistry A

Molecular insights into the in situ early-stage assembly of metal-organic frameworks on cellulose nanofibrils

Journal:	*Journal of Materials Chemistry A*
Manuscript ID	TA-ART-08-2024-005512.R1
Article Type:	Paper
Date Submitted by the Author:	28-Oct-2024
Complete List of Authors:	Zhang, Kailong; University of Tennessee, Center for Renewable Carbon Smith, Micholas; The University of Tennessee Knoxville, Biochemistry and Cellular and Molecular Biology Li, Mi; University of Tennessee, Center for Renewable Carbon

SCHOLARONE™
Manuscripts

Molecular insights into the *in situ* early-stage assembly of metal-organic frameworks on cellulose nanofibrils

Kailong Zhang, [a] Nicholas D. Smith [b] and Mi Li *[a]

The integration of metal-organic frameworks (MOFs) into renewable biopolymeric matrices, including those derived from cellulose, to create unique cellulose/MOF hybrids has attracted significant interest due to the synergistic combination of cellulose's substrate properties and MOFs' multifunctional features. The interfacial interactions between cellulose and MOF are not only responsible for the stable bonding between cellulose and MOF, but ultimately also determine the bulk physical properties of the macroscopic composites. However, the mechanistic understanding of the *in situ* assembly between the two materials remains unclear. In this study, we employ a combination strategy of synthesis, experimental characterization, and molecular dynamics simulations to explore the early-stage assembly of a cellulose/MOF hybrid. Our results reveal that the growth of MOF clusters on 2,2,6,6,-tetramethyl-1-piperidinyolxyl oxidized cellulose nanofibrils (TOCNF) follows an inhomogeneous sequential transformation pathway. The carboxylates of TOCNF form coordination-like bonds with the metal ions, while the hydroxyl groups of TOCNF form hydrogen bonds with MOF ligands. These interactions provide the initial nucleation sites that mediate the growth of MOF clusters and also guide the assembly of larger MOF clusters onto the TOCNF substrate. The fundamental insights into the *in situ* assembly of MOF nanoparticles on cellulosic substrates are essential for the rational design of high-performance materials with tailored morphology and optimized properties.

Introduction

Metal-organic Frameworks (MOFs) are a class of crystalline porous materials, synthesized through the coordination of metal ions with organic ligands.[1] MOFs have garnered increasing attention as innovative porous materials due to their remarkable surface area, tunable pore structure, and adjustable functionality.[2, 3] As such, MOFs have demonstrated a range of promising applications, including their use in water remediation [4], biomedicine [5], catalysts [6], sensors [7], conductors [8], and gas storage [9]. Nevertheless, the traditional solvothermal synthesis of MOFs often yields fine powders at a microscopic level. Their intrinsic brittleness, aqueous insolubility, and lack of plasticity pose challenges to their processability and large-scale production and application.[10-12] Growing MOFs with controlled morphology on a substrate offers a solution to achieve hybrids with improved processability and shaping for practical applications. Integrating MOFs with soft polymer materials has proven to be an effective strategy for creating 2D or 3D materials with tailored shapes and architectures..[10, 13] Cellulose nanofibrils (CNFs), in particular, are a promising biopolymer for hybridizing with MOFs due to its natural abundance, biodegradability, excellent processability, and ease of chemical modifiability.[14, 15]

MOFs are synthesized through the coordination and self-assembly of metal and ligand precursors.[2] The primary architectures, or unit cells, are constructed from basic building blocks including inorganic metal centers and organic linkers. Under controlled synthesis, these primary units assemble and grow into more complex architectures, following specific geometric patterns and connectivity, to form MOF crystals.[16, 17] When CNF is present in the synthesis system, MOFs can be *in situ* grown onto the CNF macromolecular substrate.[14] A commonly used form of CNF substrate is 2,2,6,6-tetramethyl-1-piperidinyloxy (TEMPO)-oxidized CNF (TOCNF) in which the introduced carboxyl groups on the cellulose facilitate the disintegration of cellulose fiber bundles into individual fibrils.[18] TOCNF was selected for templating MOFs due to several reasons: (1) TOCNF is a sustainable biopolymer that can be readily derived from plant cell walls. (2) The individual cellulose fibril possesses a high aspect ratio with diameters of approximately a few nanometers and lengths of several microns, providing nanoscale dimensions that are geometrically compatible with MOF nanoparticles.[19, 20] (3) The high specific surface area of TOCNF provides abundant surface carboxyl or hydroxyl groups that are accessible for interactions with MOF precursors.[14, 20] We hypothesized that the carboxyl groups can participate in the coordination sphere of the metal centers, while the hydroxyl groups can potentially form hydrogen bonds with the organic ligands in MOFs.[21, 22] The strong interactions between the CNF and MOF precursors ensure the affixation and growth of MOF particles on the substrate. The CNF-MOF interactions are crucial factors that govern the affixation and growth of MOF particles on the substrate as well as the stability

a. *Center for Renewable Carbon, School of Natural Resources, University of Tennessee, Knoxville, TN 37996, USA*
b. *Department of Biochemistry and Cellular and Molecular Biology, University of Tennessee, Knoxville, TN 37996, USA*

of combination. Coupling rigid MOF with soft biopolymer has led to the development of functional composite materials with customized shapes, such as 2D films [23, 24], 3D freestanding aerogels [20, 25] and hydrogels [26], for diverse applications. Despite these advancements in functional material fabrication, the fundamental mechanism underlying the MOF assembly dynamics on cellulose substrate remains unexplored.

Computational studies have emerged as powerful tools in advancing MOF research. These studies provide a venue to understand the fundamental mechanisms and theory, such as gas adsorption within MOF structures, thereby accelerating the discovery, design, and optimization of functional MOFs.[27-29] Moreover, computational simulations, such as molecular dynamics (MD), can offer insights into the nucleation and assembly processes during MOF synthesis. However, simulating the formation of MOFs presents challenges due to the long timescales required for the synthesis process of a complete MOF crystal, often exceeding minutes, which is extremely difficult to capture in atomic-scale simulations. Furthermore, the lack of reliable force field parameters for certain metal centers exerts extra challenge for accurate simulations.[30] Several studies have attempted to study the self-assembly process of MOFs using different modeling strategies.[31-40] For example, several endeavors involve using implicit solvents,[34] adjusting the solvent dielectric constant,[32] or employing pre-formed half-SBU precursors [39] to facilitate the simulation of MOF assembly. These strategies can partially demonstrate the ordered, interconnected topological network structure of MOFs. However, the detailed nucleation process of MOFs, especially their growth and interfacial interactions with a macromolecular substrate, has not yet been unlocked.

In this study, we first experimentally synthesized a TOCNF/MOF hybrid as a benchmark, and then employed classical all-atom MD simulations to investigate the assembly of the MOF precursors on the TOCNF substrate. We focused on the early-stage assembly of the MOF precursors at a molecular level, i.e., the interactions of a limited pool of metal ions and organic ligands, on the TOCNF substrate. The temporal evolution of MOF clusters was analyzed to understand their formation and growth dynamics. We explored the coordination-driven and hydrogen bond-driven interactions that facilitate the assembly of MOF clusters on the TOCNF substrate (**Scheme 1**). This study aims to elucidate the assembly process of MOFs on cellulose, offering mechanistic insights for the rational design of cellulose/MOF functional composites. A comprehensive understanding of this process enables the controllability over the key factors such as substrate structure, dispersion of functional groups, formulation of the synthesis, and MOF nucleation rate to ultimately tune the content, topology, and dispersion of MOF loading, and the properties of the hybrids. These designing considerations, in turn, will enhance the performance of cellulose/MOF functional composites in various applications, including adsorption, sensing, energy storage, and catalysis.

Results and discussion

Experimental synthesis

When zinc acetate is introduced, the TOCNF undergoes crosslinking to form an ionic gel. As depicted in **Fig. S1**, the crosslinked TOCNF exhibits a porous network between the fibrils. It is suggested that the Zn ions interact with the carboxylates in the TOCNF, promoting the association of chains to form junction zones.[41] Moreover, the Zn-mediated crosslinking induces electrostatic repulsion between adjacent nanofibrils due to the presence of metal cations.[42] This repulsion likely contributes to a more uniform and compact fibril alignment, with the crosslinked TOCNF exhibiting a narrower fibril width compared to the pristine TOCNF (**Fig. S1**). The FTIR spectra reveal a red shift in the crosslinked TOCNF compared to the pristine TOCNF at 1613 cm^{-1} (**Fig. S2**), which corresponds to the asymmetric stretching vibration of the carboxylates. This shift is attributed to the ionic coordination between the Zn ions and the carboxylates in TOCNF.[41]

We then combined the pre-crosslinked TOCNF with MOF precursors—Zn ions and the BDC ligands—to achieve *in situ* hybridization via a one-pot synthesis approach. The fibrous TOCNF with a high aspect ratio and nanoscale dimensions are well-suited for hybridizing MOF particles, offering geometric compatibility for templating. Zn ions and BDC can form MOF-5 crystals with a more regular cubic morphology when synthesized in the presence of water.[43] It has been reported that water molecules act as terminal ligands and participate in coordinating the Zn atoms. This coordination stabilizes the 2D pre-nucleated metal-ligand layers into well-structured crystals through hydrogen bond locking, modulating the crystal growth and enabling a more organized and hierarchical structure.[44, 45] Under the anhydrous conditions of this study, the pristine MOF exhibits an elongated and irregular crystal morphology with sizes of hundreds of nanometers (**Fig. 1a**). This observation aligns with previous studies of the synthesized MOF crystals using anhydrous zinc acetate.[46] When TOCNF is present, the *in situ* hybridization preserved the MOF structure in the TOCNF/MOF hybrid (**Fig. 1b**). Meanwhile, the hybrid exhibits a more aggregated morphology, with the crystal particles embedded and affixed within the TOCNF network. This
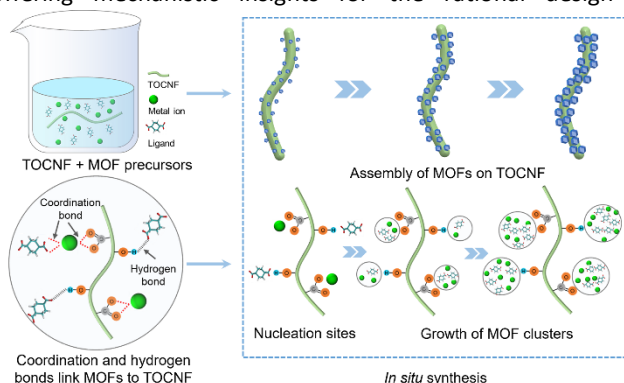
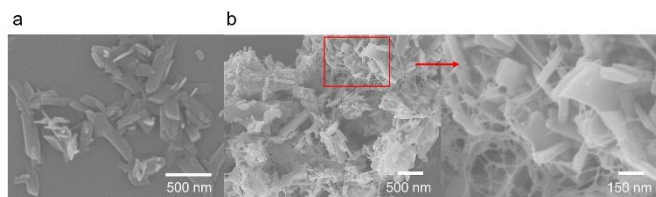Scheme 1 Illustration of the MOF assembly process on TOCNF.

Fig. 1 SEM images of Zn-BDC MOF (a) and TOCNF/MOF hybrid (b).

morphological characterization suggests suitable templating compatibility of TOCNF and MOF at the nanoscale.

The FTIR absorbance bands at 1580 cm^{-1} and 1376 cm^{-1} correspond to the stretching vibrations of carboxylate primarily in the BDC ligand (**Fig. S2**).[43] The bands at 815 cm^{-1} and 749 cm^{-1} vibrations in the disubstituted rings of the BDC ligand.[46] The FTIR peaks of the pristine MOF are identical in the spectrum of the TOCNF/MOF hybrid. The band at 3350 cm^{-1} corresponds to the stretching vibrations of -OH groups and the band at 2900 cm^{-1} is attributed to the symmetric stretching -CH$_2$ vibrations in the TOCNF. These spectroscopic results confirm that the TOCNF/MOF maintains the characteristic features of both cellulose and MOF.

The pristine MOF and TOCNF/MOF hybrid exhibit similar XRD patterns (**Fig. S2**), indicating the presence of identical MOF phases in both materials. The characteristic peaks of cellulose crystals are not discernible in the TOCNF/MOF hybrid pattern. This is attributed to the TOCNF fibers exhibiting significantly lower diffraction intensity compared with the MOF. The characteristic peaks of the MOF-5 crystal phase, typically

reported at 2θ of 6.9°, 9.7°, 13.7°, and 15.3°,[47] were not observed in the current results, suggesting that the MOF-5 phase was likely not formed under the anhydrous synthesis conditions. A prominent peak at 2θ of 8.88° was observed, which aligns with previous studies of the synthesized MOF in the absence of water.[46] These spectroscopic results validate the experimental feasibility of *in situ* hybridizing TOCNF and MOF and will serve as a benchmark for the subsequent MD simulations.

Local coordination environment of Zn ions

Zn ions and BDC ligands are the primary precursors in the synthesis of MOFs, such as MOF-2 with a square lattice and MOF-5 characterized by a cubic lattice.[48] The complete crystallization of MOF synthesis typically spans several hours for nucleation and crystal growth. This extended timescale presents significant challenges for atomic-level simulation, particularly in our case where the system necessitates a large simulation box for TOCNF. Therefore, we have confined our simulation to 150 ns trajectory length and focused on the early stages and molecular level interactions of Zn and BDC during self-assembly in the presence of TOCNF. We note that a smaller simulation box has been conducted with an extended time to 500 ns to ensure convergence. We analyzed the cluster formation (with a detailed cluster analysis provided in the following section) and observed that the system converged within 5 ns (**Fig. S5**).

We first studied the coordination environment of Zn ions. The coordination sphere encompasses DMF solvent molecules, acetate counterions, and BDC organic ligands. The radial
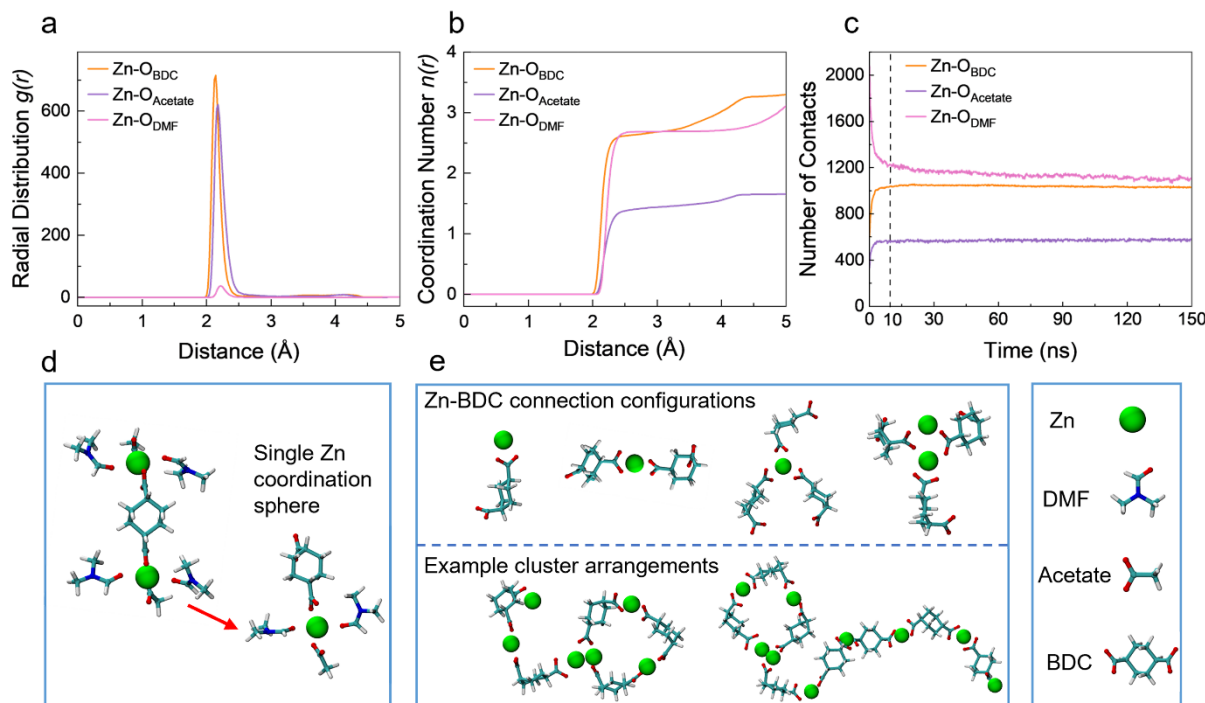

Fig. 2 Analysis of Zn ion coordination environments: radial distribution function (a), coordination number (b), and the number of contacts between Zn ions and oxygen atoms in BDC, acetate, and DMF, respectively (c). Radial distribution function and coordination number is calculated from 140 ns to 150 ns. Snapshots depicting the local coordination environment of Zn ions, with the single Zn coordination sphere shown on the right (d). Snapshots depicting typical connection configurations between Zn ions and BDC at the top, and two exemplary cluster arrangements at the bottom (e). Analysis and snapshots are derived from the S$_{MOF}$ system.

distribution functions (RDFs) of Zn ions with respect to oxygen (O) atoms in BDC, acetate, and DMF were calculated. As shown in **Fig. 2a**, the RDF exhibits distinct peaks at 2.13 Å for Zn-O in BDC, 2.18 Å for acetates, and 2.22 Å for DMF. These peaks indicate that the specific coordination distances between Zn ions and O atoms in each molecule are in the order of BDC < acetate < DMF. Within a single local coordination sphere, a Zn ion can engage approximately six O atoms. The coordination number (**Fig. 2b**), derived from the integration of RDF curves, indicates that a single Zn ion is capable of coordinating with two to three O atoms in BDC or DMF, and with one to two O atoms in acetate.

We have found that the assembly process of MOFs involves more than Zn and BDC. The DMF solvent and the counterion acetate also play crucial roles. **Fig. 2d** demonstrates a representative coordination snapshot taken from the S_{MOF} system at 150 ns, illustrating how the carboxyl groups in BDC ligands bind with Zn ions, while the O atoms in acetate and DMF molecules occupy the remaining coordination sites. We further analyzed the number of contacts between Zn and O atoms in BDC, acetate, and DMF. Contact is defined as less than 2.5 Å between atoms, based on the RDF results. As depicted in **Fig. 2c**, the total number of contacts between Zn and O atoms in BDC and acetate rises significantly within the first 10 ns, and subsequently stabilizes. Conversely, the number of contacts between Zn and O atoms in DMF initially shows a high count, then significantly decreases before 10 ns, followed by a gradual declining trend. We infer that during MOF assembly, DMF solvent molecules may act as pseudo-ligands, readily "binding" to Zn ions through weak coordination. Over time, the bound DMF gradually disassociated from the Zn ions, liberating coordination sites for the carboxyl groups in BDC or acetate. As Zn's coordination sites become increasingly occupied, DMF molecules are gradually released back into the solvent system. This reversible participation of DMF agrees well with the observations from a previous study, which demonstrated the dynamic coordination of DMF solvent molecules with Zn ions.[49] Therefore, the role of DMF in the MOF synthesis process extends beyond merely solubilizing the components to facilitate chemical transformations; a certain amount of DMF molecules also participate in the reversible binding with metal ions as solvent ligands, aiding the ligand exchange process.[50] Simultaneously, the acetate counterion interacts with the metal center to balance the electrostatic charge. We observed that the carboxyl groups in acetate cap the coordination sphere and then exchange with the BDC ligand, facilitating cluster growth. The curve of the Zn-$O_{Acetate}$ contact number shows an initial rise followed by a leveling off, stabilizing after about 10 ns (**Fig. 2c**). We propose that the acetate anions act as exchangeable templating ligands, fixing the Zn coordination in a favorable state. These acetate counterions facilitate the Zn-BDC cluster assembly by initially occupying coordinatively unsaturated sites on Zn ions, subsequently exchanging with free BDC ligands.[51] This coordination enables various types of topological connections and configurations between Zn and BDC. **Fig. 2e** depicts the typical topological configurations of Zn-BDC observed in the system. One single Zn ion can serve as a vertex

to bridge one, two, or three carboxylates in BDC ligands. Moreover, two Zn ions can pair together and bridge three carboxylates. These diverse connecting units further assemble into clusters with the additional participation of Zn ions and BDC ligands, resulting in different fragment arrangements in 1D, 2D, or 3D structures, exhibiting circular or fibrous connections (**Fig. 2e**).

Cluster evolution

We then analyzed the temporal evolution of the Zn-BDC MOF clusters. To identify and search for clusters, we employed the connected components using graph theory through in-house Python code.[52] As illustrated in **Fig. S3**, a set of Zn nodes and BDC ligands are considered to constitute a connected component (cluster) if any node within this set can reach any other node through a connecting path. The Zn and BDC nodes are considered paired (form a path) if the distance between them is shorter than 2.5 Å, a cutoff distance determined based on the RDF analysis. The size of a cluster is defined by the count of Zn ions it comprises. For instance, a cluster is designated as a size of 19 because it contains 19 Zn ions (**Fig. S4**). We then evaluated the distribution of Zn ions across different cluster sizes. This distribution was assessed by calculating the proportion of Zn, defined as the ratio of the total number of Zn ions in each cluster type to the total number of Zn ions in the system. This approach provides a view of cluster evolution and the dynamic interaction between Zn ions and BDC ligands in the system.

In the pristine S_{MOF} system, the fraction of free Zn ions exhibits a rapid decline within the initial 10 ns (**Fig. 3a**) due to the increasing involvement of Zn ions in cluster formation with BDC at the beginning. This observation agrees with the results of Zn-BDC coordination shown in **Fig. 2c** in which the contact number between Zn ions and O atoms in BDC rises rapidly at the beginning stage. Moreover, the distribution of Zn ions shifts from smaller clusters to larger clusters over time, with an increasing proportion of Zn found in these larger clusters (**Fig. 3a**). In the beginning 10 ns, the proportion of Zn in the smaller clusters of sizes 1-4 experiences a significant reduction, suggesting these clusters act as intermediates that subsequently evolve into larger clusters. Subsequently, larger clusters emerge and grow at a later stage. We also observed the dynamic evolution of cluster formation and disappearance. For instance, the cluster of size 19 appears at 99 ns but diminishes at 114 ns, at which point a cluster of size 20 emerges. These observations indicate that the cluster evolution is a dynamic reconfiguration and inhomogeneous sequential growth rather than simple amplification. The evolution of cluster sizes stabilizes after 114 ns. By the end of the simulation at 150 ns, approximately 14% of Zn ions remain unbound as free ions, whereas 86% of them are assembled into the clusters with BDC. Throughout the simulation, a total of 13 distinct cluster sizes are identified, with 12 persisting at 150 ns, and the largest cluster size reaching 20. Clusters of sizes 2, 3, 4, and 7 exhibit a relatively higher proportion of Zn. We then quantified the frequency of each cluster size at 150 ns (**Fig. S6**). We found that smaller clusters, such as sizes 1 to 4, exhibit a higher frequency

with each exceeding 15. In contrast, larger clusters, including sizes 9, 10, and 20, are less frequent with each occurring only once. These observations corroborate the heterogeneous formation and reconfiguration of Zn-BDC clusters.

We also examined the cluster evolution in the $S_{Hybird-5}$ system, which contains a similar number of precursors compared to S_{MOF} but includes one additional TOCNF (**Table S2**). As shown in **Fig. 3b**, the overall temporal evolution of Zn ions is similar to that in the pristine S_{MOF} system. We note that the distribution of Zn ions in $S_{Hybird-5}$ also includes a fraction of Zn ions exclusively coordinated with TOCNF (with a detailed coordination analysis to be discussed subsequently). To monitor and compare the dynamic differences in cluster evolution between the two systems, we adopted a statistical approach to model the distribution of Zn ions in different cluster fractions over time, assuming this distribution reaches an equilibrium state as time progresses. We calculated the total variation distance between the current distribution and the equilibrium distribution at each time step, considering the latter as the distribution at the end of the simulation to assess the evolution speed:

$$\delta(P, Q) = \frac{1}{2} \sum_x |P(x) - Q(x)|$$

where $P(x)$ is the current probability mass function and $Q(x)$ is the equilibrium probability mass function. We observed that the total variation distance in both SMOF and SHybrid-5 systems decreases rapidly during the initial 45 ns (**Fig. 3c**), indicating that most Zn ions are quickly distributed among various clusters. Interestingly, Zn ions in SHybrid-5 systems reached equilibrium earlier (103 ns) compared to those in the SMOF system (114 ns).
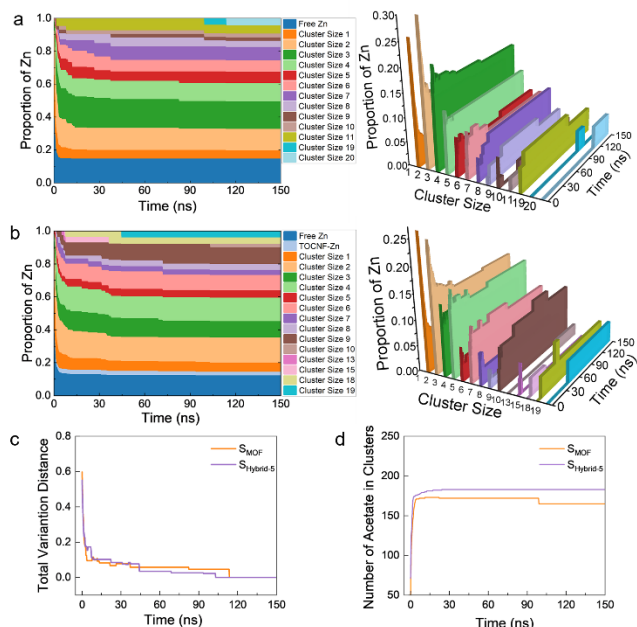

Fig. 3 The distribution of Zn ions in different cluster fractions over time in S_{MOF} (a) and $S_{Hybird-5}$ (b) systems. The total variation distance of the Zn ion distribution in S_{MOF} and $S_{Hybird-5}$ systems (c). Number of acetate molecules in the MOF clusters in S_{MOF} and $S_{Hybird-5}$ systems (d). "Free Zn" refers to the Zn ions not interacting with BDC or TOCNF, and "TOCNF-Zn" refers to the Zn ions exclusively interacting with TOCNF. The cluster size is determined by the number of Zn ions it contains. The proportion of Zn is calculated as the ratio of the Zn number in each fraction to the total Zn number in the system.

This observation suggests that the cluster evolution in the TOCNF-containing system ($S_{Hybird-5}$) may be, albeit slightly, accelerated in comparison to the S_{MOF} system.

We compared the number of acetate molecules present in the clusters of both the S_{MOF} and $S_{Hybird-5}$ systems. An acetate molecule is considered attached to the cluster if the distance between the acetate and Zn ions in the cluster is less than 2.5 Å. As shown in **Fig. 3d**, the number of acetates in the S_{MOF} system rises rapidly at the beginning and then slowly decreases as the MOF clusters grow. However, in the $S_{Hybird-5}$ system, no significant decrease in the number of acetates is observed after the initial rise. Meanwhile, we observed that the number of contacts of the O atoms in the carboxylates of TOCNF with Zn ions gradually increased over time (**Fig. S8**, the contact analysis is provided in the following section). We infer that some of the acetates in the $S_{Hybird-5}$ system are replaced by the carboxylates of TOCNF, leading to a less significant decrease in the contact number compared to the S_{MOF} system. The carboxylates in TOCNF can serve as a modulating ligand, similar to acetate, to cap the unsaturated coordination sphere of Zn. These carboxylates may anchor the MOF clusters and serve as nucleation sites to modulate the cluster growth.

We performed *in situ* liquid-state ^{1}H NMR to monitor the real-time reaction of MOF synthesis in the liquid phase (**Fig. 4**). As the synthesis progresses, soluble precursor molecules in the liquid phase transform into the solid MOF crystal phase. Therefore, the *in situ* monitoring of the changes in the liquid phase substances provides additional real-time evidence for cluster formation. The NMR signal of BDC ligands was not observed in the solution, likely due to the low BDC/Zn ratio of 0.5. This ratio caused most BDC molecules to rapidly engage with Zn ions, transforming into a solid phase that made BDC nondetectable by liquid-state NMR. However, the spectra of DMF and acetate were well monitored and acquired. In the ^{1}H NMR spectra, two quintets centered at 2.92 and 2.75 ppm and a singlet at 8.03 ppm were identified for DMF. The signal peak at 1.90 ppm was identified for acetate. Our time-resolved NMR experiments reveal that the peak intensities for DMF and acetate gradually increased over time before stabilizing at about 100 minutes, indicating their concentrations were increasing in the solution. Moreover, the real-time changes in peak intensity for both molecules occurred concurrently. These results suggest that DMF and acetate participated in the MOF synthesis, and they were being exchanged and released back into the solvent phase over time, which aligns with our simulation findings shown in **Fig. 2**. We also note that at least two inflection points in the NMR peak intensity curves were observed during the intensity increase phase (shaded regions in the right of **Fig. 4**). According to Ostwald's rule, sequential transformations are often necessary to crystallize the final MOF products.[53] We contend that these downward knees result from the dissolution-recrystallization reactions of the metastable phase during MOF formation. In this process, the dissolution of the reactant phases could release reactive species into the solution, which then form more thermodynamically stable product phases.[54, 55] The time-resolved ^{1}H NMR results also demonstrate that the incorporation of TOCNF accelerated the

release of DMF and acetate. As shown in **Fig. 4**, both DMF and acetate in the hybrid system reached equilibrium faster (~75 minutes) than the pristine MOF system (~105 minutes). The accelerated release of DMF and acetate implies a quicker exchange with BDC molecular ligands thereby a more rapid formation of MOF clusters. We note that the ratio of Zn ions to BDC remains consistent at 2:1 in the simulation of the bench synthesis experiment. The overall concentrations in the simulation are about 10 times higher than those in the experiment due to the dimensional constraints of the simulation box. Moreover, the simulation focuses on the early stages of assembly (within 150 ns) due to computational limitations, whereas the experimental process spans several hours to capture more discernible synthesis changes. Despite the scale difference, the experimental observations align well with the simulation results. Real-time NMR studies confirmed that the DMF solvent and acetate counterions participate in the MOF synthesis process. This behavior, captured both in experiment and simulation, suggests that these molecules are active parts of the coordination environment of Zn ions, modulating MOF cluster formation. Additionally, our computational data suggest the presence of TOCNF accelerates the formation of MOF (**Fig. 3**), which deserves further investigation. Interestingly, however, our follow-up NMR work also indicates a faster exchange of DMF and acetate, consistent with our simulations.
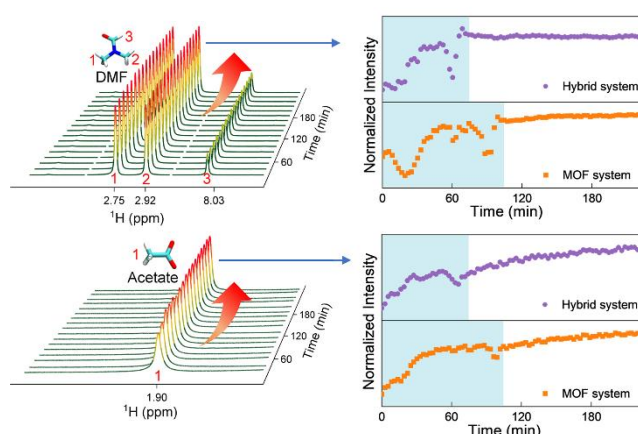

Fig. 4 Stacked liquid-state ^1H NMR spectra of DMF and acetate over time (left) and the normalized intensity of the NMR peaks for DMF at 2.92 ppm and acetate at 1.90 ppm over time (right). NMR data were collected from the MOF synthesis solution and the TOCNF/MOF hybrid solution at 25℃, each containing 43% (v/v) DMF-d_7.

Cluster attachment on TOCNF

The carboxylates on the TOCNF surface can participate in the coordination environment of Zn ions, serving as binding sites and modulating the growth of Zn-BDC MOF clusters (**Fig. 5a**). We analyzed the RDF between Zn ions and the O atoms in the carboxylates of TOCNF. As depicted in **Fig. S8**, the RDF curve demonstrates the coordination bond between the Zn ion and the carboxylates of TOCNF at 2.17 Å. This coordination distance is comparable to that observed between Zn and the carboxyl groups of BDC, which is determined at 2.13 Å. We then

examined the number of contacts between Zn ions and the O atoms in the carboxylates of TOCNF, setting a cutoff distance of 2.5 Å as inferred from the RDF analysis. The quick increase in the number of contacts indicates that Zn ions rapidly interact with the carboxylates on TOCNF within the first 10 ns. Subsequently, the number of contacts approaches an equilibrium (**Fig. S8**). The coordination between TOCNF and Zn ions could potentially create anchoring sites that facilitate the assembly of Zn-BDC clusters on the TOCNF substrate.

We then examined the attachment of Zn-BDC clusters to TOCNF through coordination. A cluster is considered attached to TOCNF if at least one Zn in the cluster is within 2.5 Å of the O atoms in the carboxylates of TOCNF. **Fig. 5b** depicts the temporal evolution of the Zn distribution in clusters attached to TOCNF through coordination. The accumulation of Zn ions on the TOCNF via coordination increases over time. The initial attachment begins with the smaller clusters. Within the first 4 ns, the attached clusters are smaller than size 4. Over time, the pre-formed small cluster intermediates (i.e., clusters smaller than 4) grow and evolve into larger clusters by accumulating more Zn ions and BDC on the pre-existing clusters already bound with TOCNF. For example, at 72 ns, the proportion of Zn in size 3 clusters decreases, while the proportion of Zn in size 4 clusters simultaneously increases, indicating a transition from size 3 to size 4 clusters. Furthermore, at 103 ns, the proportion of Zn in size 9 clusters decreases, and a new cluster size, size 10, appears. These observations indicate that the attachment of clusters to TOCNF occurs through an *in situ* assembly and continuous growth process, suggesting that the clusters form directly on the TOCNF rather than through the post-addition of pre-assembled clusters. We also observed that a small proportion of Zn ions (2.2%) exclusively coordinated with TOCNF without forming clusters with BDC (**Fig. 3b**). This indicates that certain carboxylates on TOCNF are occupied by
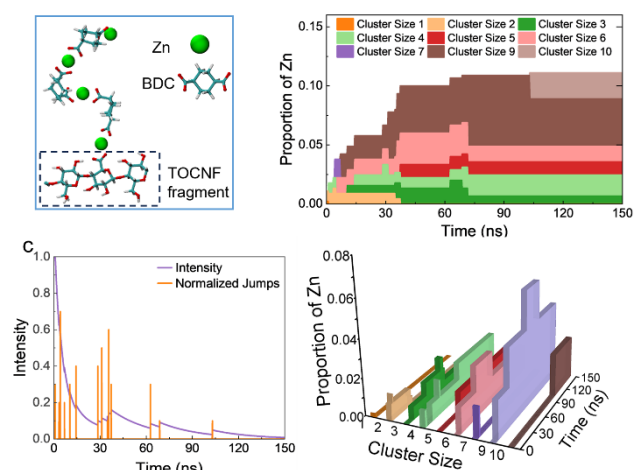

Fig. 5 Snapshot depicting the coordination between MOF clusters and TOCNF (a). Time evolution of Zn ion distribution in different cluster fractions attached to TOCNF via coordination (b). Normalized jumps of the arrival of Zn ions onto the TOCNF and the conditional intensity function for the Hawkes process (c). The cluster size is determined by the number of Zn ions it contains. The proportion of Zn is calculated as the ratio of the Zn number in each fraction to the total Zn number in the system. Analysis and snapshot are derived from the $S_{Hybrid-5}$ system.

single Zn ions, instead of Zn-BDC clusters, suggesting that not all carboxylates of TOCNF participate in anchoring MOF clusters. The proportion of Zn attached to the TOCNF stabilizes after 103 ns, with approximately 11% of the Zn ions assembled on the TOCNF. Among these, clusters of size 9 account for the largest proportion (**Fig. 5b**). By the end of the simulation at 150 ns, clusters of sizes 3, 4, 5, 6, 9, and 10 were observed to be attached to the TOCNF. The frequency of these clusters at 150 ns is presented in **Fig. S9**. Each identified cluster size exhibits a low frequency of less than 2, which likely results from the limited availability of carboxylates on the TOCNF for MOF anchoring.

The arrival of Zn in MOF clusters on TOCNF through coordination bond demonstrates a temporal clustering phenomenon. To capture this phenomenon, we employed the Hawkes process, a non-Markovian extension of the Poisson process capable of modeling random events that exhibit self-exciting behavior.[56, 57] We modeled the arrival of Zn ions onto the TOCNF using a Hawkes process $N(t)$ with an exponentially decaying base intensity to further reflect the mixing to equilibrium in the system. A jump occurs in the process when new Zn ions aggregate on the TOCNF. **Fig. 5c** illustrates that these jumps exhibit a decaying base intensity and temporal clustering. To account for both phenomena, we assume that the total intensity function $\lambda^*(t)$ for the Hawkes process takes the form:

$$\lambda^*(t) = \lambda e^{-\beta_1 t} + \mu * N(t)$$

where $\mu(t) = \alpha e^{-\beta_2 t}$, $N(t)$ is the point process, and * denotes the convolution operator. The model parameters are found using maximum likelihood estimation. To evaluate the appropriateness of the proposed model, we conducted a goodness-of-fit test [58] using the estimated parameters and found a p-value of 0.91, allowing us to retain the null hypothesis. The estimated intensity function is plotted in **Fig. 5c**. A high function intensity was observed within the first 45 ns, suggesting the arrival of Zn is more favorable. Over time, the intensity probability of Zn attaching to TOCNF decays, indicating that the Zn aggregation becomes increasingly difficult.

The attachment of MOF clusters onto TOCNF is not solely driven by coordination effects but also facilitated by hydrogen bonds between BDC ligands and TOCNF. This interaction is formed between the hydroxyl groups on TOCNF, which act as hydrogen bond donors, and the acceptor O atoms in BDC ligands (**Fig. 6a**).[59] We examined the formation of hydrogen bonds between the hydroxyl groups at oxygen atoms O2, O3, and O6 in TOCNF and the oxygen atoms in BDC. Here, O2, O3, and O6 correspond to the oxygen atoms at carbon positions 2, 3, and 6 on the glucose ring, respectively. For the analysis of hydrogen bonds, we used a donor-acceptor cutoff distance of 3.5 Å and a cutoff angle of 30°. As depicted in **Fig. 6b**, all the oxygen atoms O2, O3, and O6 can engage in the formation of hydrogen bonds with BDC ligands. The number of hydrogen bonds formed by O6 atoms is slightly lower than those formed by O2 and O3. This difference could be attributed to the conversion of 36 hydroxyl groups at the O6 position into carboxylates in the TOCNF model. The total number of hydrogen bonds formed by the three atom

types shows a slight increasing trend before 40 ns and then stabilizes at around 55 ns. These results suggest that the hydrogen bond could potentially serve as an anchoring site, facilitating the attachment of MOF clusters to TOCNF.

We then evaluated the attachment of MOF clusters to TOCNF mediated by hydrogen bonds. A cluster is considered attached to TOCNF when at least one BDC ligand in the cluster forms a hydrogen bond with TOCNF, and the Zn ions in these clusters do not have any coordination interaction with TOCNF. We note that some clusters can interact with TOCNF through both coordination and hydrogen bonds. In such cases, we classify the attachment as coordination driven. **Fig. 6c** depicts the time evolution of the Zn distribution in the clusters that are attached to TOCNF by hydrogen bonds. Some clusters, such as size 5, exhibit a dynamic attachment and detachment (red area in **Fig. 6c**). We hypothesize that this phenomenon is due to the weak interactions of hydrogen bonds, which are insufficient to tightly hold the clusters.
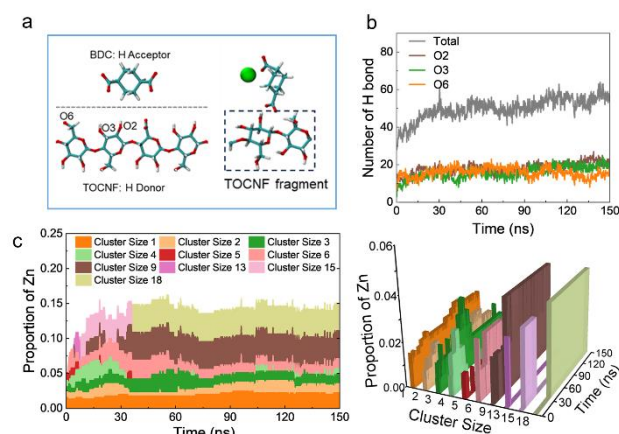

Fig. 6 Illustration of the interaction sites between the hydrogen bond donor of TOCNF and acceptor of BDC ligand, and snapshot depicting the hydrogen bond between MOF clusters and TOCNF (a). Number of hydrogen bond formed between the hydroxyls at O2, O3, and O6 in TOCNF and the oxygen atoms in BDC (b). Time evolution of Zn ion distribution in different cluster fractions attached to TOCNF via hydrogen bond (c). The cluster size is determined by the number of Zn ions it contains. The proportion of Zn is calculated as the ratio of the Zn number in each fraction to the total Zn number in the system. Analysis and snapshot are derived from the S$_{Hybrid-5}$ system.

The snapshots of the hybrid system at different simulation stages are present in **Fig. 7a-e**. The visualized results demonstrate the gradual formation and assembly of MOF clusters on TOCNF. All precursor molecules are initially freely distributed within the simulation box. Over time, Zn ions and BDC ligands engage in the formation of MOF clusters, with some of these clusters attached to the TOCNF. We then evaluated the distribution of Zn ions within clusters attached to TOCNF through coordination and hydrogen bonds, as well as those free clusters not attached to the TOCNF. As shown in **Fig. 7f**, approximately 85% of Zn ions engage with BDC to form clusters in the S$_{Hybrid-5}$ system. About 10% of Zn ions accumulate on TOCNF through coordination-driven cluster assembly, while about 15% attachment is via hydrogen bond. The rest 60% of Zn ions remain in clusters that are not attached to the TOCNF.

Classical nucleation theory has provided a theoretical framework for understanding the mechanisms of MOF
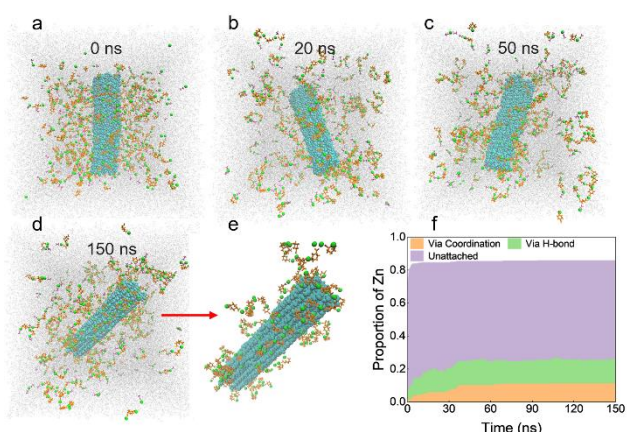
Fig. 7 Evolution of the $S_{Hybrid-5}$ system captured at different stages (a-d highlight cluster sizes). Snapshot showing MOF clusters attached on the TOCNF at 150 ns (e). Color coding: grey for DMF, green for Zn ions, yellow for the BDC ligand, mauve for acetate, and cyan for TOCNF. Distribution of Zn ions in clusters attached to TOCNF (via coordination and hydrogen bonds) and free clusters not attached to TOCNF (f). The proportion of Zn is calculated as the ratio of the Zn number in each fraction to the total Zn number in the system. Analysis and snapshots are derived from the

crystallization.[55, 60, 61] This theory relies on the assumption that growth from solution occurs via the diffusion and subsequent incorporation of small monomeric units onto the crystal surface. In this view, the MOF growth is seen as an amplification process where stable nuclei are enlarged by unit-cell replication without structural changes in the bulk or at the surface. However, in multicomponent systems with a variety of intermediates during MOF synthesis, these assumptions can be violated. Therefore, the crystallization process is more commonly proposed to follow a non-classical nucleation process. Under the assumption of non-classical nucleation theory, the original 0D monomeric MOF precursors first are assembled into pre-cluster intermediates. These low-dimensional MOF intermediates can then evolve into more complex 2D and 3D crystalline materials (**Fig. 8**).[62, 63] In both the pristine MOF system and the Hybrid system of our simulation, we observed that the initial free Zn ions in the solution can rapidly engage with the BDC to form small clusters, e.g., cluster size 1-4, at the beginning stage and then these small clusters act as pre-cluster intermediates and evolve into larger cluster sizes with more complex architectures. Our simulation demonstrates that the cluster growth follows inhomogeneous sequential transformations rather than a direct nuclei amplification process, aligning with the non-classical nucleation theory. In the meantime, the DMF solvent and acetate counterions influence cluster formation by modulating the coordination environment of the metal ions. The DMF molecules function as pseudo-ligands, initially binding to the Zn ions and subsequently being released and exchanged during cluster formation and growth. Likewise, the acetate counterions act as templating ligands, capping the unsaturated coordination sphere of Zn ions and being exchangeable with BDC during cluster growth. Notably, the MOF clusters interact with the TOCNF macromolecular substrate through hydrogen bonds and coordination bonds (**Fig. 8**). We propose that the coordination interaction mediates the MOF cluster formation. Zn ions quickly bind to the carboxylates

on the TOCNF, after which the pre-cluster intermediates engage with the existing Zn on the TOCNF surface, which then attracts additional pre-cluster intermediates to promote sequential cluster growth. The TOCNF surface provides nucleation sites for cluster growth, likely accelerating cluster formation.
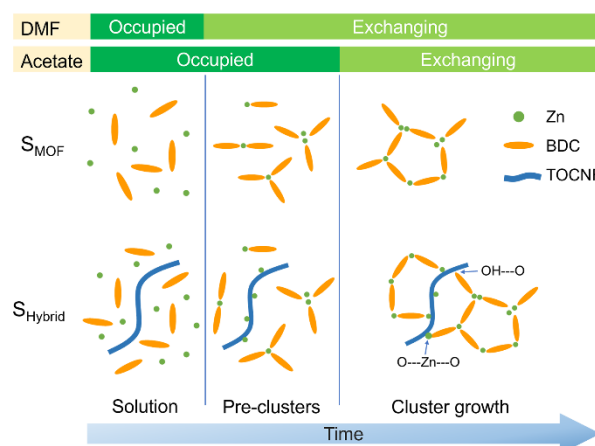

Fig. 8 Illustration of the MOF cluster formation and its interaction with TOCNF at early stage.

Effect of metal/ligand ratio and precursor concentration

The formation and attachment efficiency of MOF clusters on TOCNF are influenced by the ratio of metal to ligand and their concentrations. We investigated the impact of different metal-to-ligand ratios in three simulation systems by varying the number of Zn ions while keeping the number of BDC ligands constant. This approach resulted in three systems: $S_{Hybrid-1}$ (Zn:BDC = 11:8), $S_{Hybrid-2}$ (Zn:BDC = 13:8), and $S_{Hybrid-3}$ (Zn:BDC = 15:8), representing a range from low to high metal content. As shown in **Fig. 9a**, a higher Zn/BDC ratio ($S_{Hybrid-3}$) tends to form larger sizes of MOF clusters. This is attributed to the increased concentration of Zn ions, which enhances the likelihood of coordination between Zn and preformed clusters, thereby facilitating cluster growth. Additionally, systems with lower Zn/BDC ratios exhibited a higher proportion of total cluster formation (**Fig. 9b**). This is likely due to the lower proportion of Zn ions, which leads to a higher coordination probability per Zn ion, thereby increasing the likelihood of Zn ions being transformed into MOF clusters. The lower ratio system also promotes the coordination-driven cluster attachment on TOCNF, as seen in **Fig. 9b** a higher proportion of Zn attached to TOCNF via coordination in $S_{Hybrid-1}$. We infer that with a constant number of anchoring sites (i.e., carboxylates) on TOCNF, a lower overall concentration of Zn ions is more favorable for engaging with both BDC to form clusters and the carboxylates on TOCNF to be attached. No obvious differences are observed in hydrogen bond-driven attachment among the three systems, which could be attributed to the consistent number of BDC ligands across these systems.

We then examined the effect of precursors' concentrations among systems $S_{Hybrid-2}$, $S_{Hybrid-4}$, and $S_{Hybrid-5}$, with increasing concentrations in a ratio of 1:2:4 based on the number of BDC ligands. As shown in **Fig. S11**, higher precursor concentrations yield larger cluster sizes ($S_{Hybrid-5}$ > $S_{Hybrid-2}$ > $S_{Hybrid-4}$). This is because an increase in precursor concentration enhances the diffusion rates and the coordination probability, which in turn promotes cluster growth.[64] A higher precursor concentration also promotes the transformation of more Zn ions into clusters, as evidenced by the higher proportion of Zn ions in the total clusters in $S_{Hybrid-5}$ (**Fig. S11**). Additionally, we observed that in systems with lower precursor concentrations, a greater proportion of Zn ions accumulate on TOCNF through coordination bonds. The number of available coordination sites on the TOCNF surface remains constant across these systems. Consequently, the potential of clusters binding to TOCNF remains relatively stable. We infer that in systems where fewer clusters are formed, the relative proportion of clusters attaching to TOCNF increases.
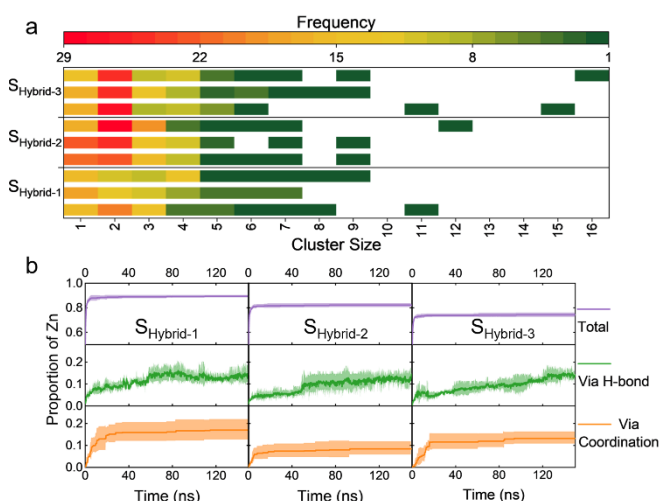

Fig. 9 Effect of different metal/ligand ratios on the formation of cluster sizes at 150 ns. Data are presented as three individual replicates for each system (a). Effect of the metal/ligand ratio on the distribution of Zn ions in various cluster fractions. The yellow line represents clusters attached to TOCNF via coordination bond, the green line represents clusters attached to TOCNF via hydrogen bond, and the purple line represents the total clusters formed in the system. Data are presented as mean ± standard deviation from three replicates (b). The analysis is based on the $S_{Hybrid-1}$, $S_{Hybrid-2}$, and $S_{Hybrid-3}$ systems, with metal to ligand ratios of 11:8, 13:8, and 15:8, respectively.

Conclusions

In this study, we have conducted all-atom MD simulations to investigate the assembly of MOF precursors and their interaction with TOCNF at the molecular level, by closely mimicking experimental synthesis conditions. The coordination environment of Zn ions reveals that both DMF solvent and acetate anions participate in the coordination sphere of the metal, facilitating the assembly between Zn ions and BDC ligands. This coordination leads to the formation of MOF clusters with various topological units and arrangements. The time evolution of Zn ions demonstrates that the formation of MOF clusters is a dynamic process involving continuous growth

and reconfiguration. Over time, small pre-cluster intermediates evolve into larger clusters. This cluster growth process follows inhomogeneous sequential transformations, consistent with the non-classical nucleation theory. The MOF precursors interact with the TOCNF, where metal ions form coordination bonds with the carboxylates of the TOCNF, and BDC ligands form hydrogen bonds with its hydroxyl groups. These interactions direct the *in situ* assembly of MOF clusters onto the TOCNF. The TOCNF macromolecule substrate also potentially mediates MOF growth, with its carboxylates providing nucleation sites that likely facilitate cluster formation. Furthermore, we observed that the metal-to-ligand ratio and their concentrations significantly influence the attachment efficiency. We note that our simulations are limited to the early stages of assembly and do not capture the complex MOF architecture beyond the molecular level, as well as involving only a single TOCNF and not considering inter-fiber crosslinking between CNF fibrils. Future work, such as coarse-grained simulations, could be deployed to explore the entire assembly process of MOF on cellulose fibers and provide a more detailed understanding of the complex MOF architecture and even MOF crystals. Additionally, multiple TOCNF fibers and potential inter-fiber interactions (i.e., hydrogen bonding and crosslinking) between CNF fibrils should be considered to better capture the structural dynamics of cellulose-MOF interactions at a macroscopic level.

Experimental section

Experimental synthesis and characterizations

CNF with 3.1 wt% concentration in an aqueous slurry was purchased from the United States Department of Agriculture's Forest Products Laboratory (FPL, Madison, WI) and acquired through the Process Development Center in the University of Maine (Orono, ME, USA). Sodium bromide (NaBr), sodium hypochlorite (NaClO), 2,2,6,6-tetramethyl-1-piperidinyloxy (TEMPO), zinc acetate dihydrate ($Zn(OAc)_2 \cdot 2H_2O$), terephthalic acid (BDC), dimethylformamide (DMF), and deuterated DMF (DMF-d_7) were purchased from Fisher Scientific. Anhydrous zinc acetate ($Zn(OAc)_2$) was prepared by drying $Zn(OAc)_2 \cdot 2H_2O$ at 110 °C for 4 hours. All the chemicals were analytical grade.

TOCNF was prepared following the reported methods with some modifications.[65, 66] Briefly, 0.15 g TEMPO and 1.5 g NaBr were added in 1 L of 1 wt% original CNF suspension. The pH of the resulting mixture was adjusted to 10.5. The oxidation reaction was initiated by adding 25 mmol NaClO. The mixture was stirred at 150 rpm at room temperature for 5 hours, with the pH maintained at 10.5. After the reaction, the oxidized CNF was washed with DI water through filtration, followed by disintegration using a high-speed homogenizer (IKA Ultra-Turrax) at 10000 rpm for 30 minutes. The TOCNF was collected as the supernatant after centrifugation at 10000 g for 20 minutes. The morphology of the TOCNF is provided in **Fig. S1**. The carboxylate content was measured to be 0.7 ± 0.03 mmol/g using the conductometric titration method.[67]

The TOCNF was first crosslinked by adding 1 g of Zn(OAc)$_2$ to 20 mL of 0.1 wt% TOCNF suspension and stirring at room temperature for 1 hour. Next, the mixture was washed twice with water and three times with DMF using centrifugation at 8000 g for 10 minutes each. The crosslinked TOCNF was then redispersed in 10 mL DMF to achieve 0.2 wt% concentration. The SEM image of the crosslinked TOCNF is shown in **Fig. S1**.

The synthesis of the TOCNF/MOF hybrid was carried out using a modified process of a reported method.[46] Specifically, 0.085 g of BDC and 0.18 g of Zn(OAc)$_2$ were dissolved in 5 mL DMF, respectively. The Zn(OAc)$_2$ solution was gradually added into the previously prepared 10 mL of 0.2 wt% TOCNF suspension in DMF, followed by the gradual addition of the BDC solution. The mixture was then subjected to a reaction at 121 ℃ for 2 hours in an autoclave. Following the reaction, the resultant hybrid product was collected and washed twice with DMF and twice with water using centrifugation at 8000 g for 10 minutes each. For comparison, a pristine MOF without TOCNF was synthesized using the same procedure.

Micro-morphology was characterized using a scanning electron microscope (SEM, Zeiss, Auriga). The samples were sputtered with gold prior to observation. The X-ray diffraction (XRD) patterns were collected using an X-ray diffractometer (PANalytical Empyrean) operating at 45 kV and 40 mA. The diffractograms were obtained at a scan rate of 4°·min^{-1} and a step size of 0.02°. Fourier transform infrared (FTIR) spectra were recorded using a PerkinElmer spectrometer. Samples were prepared as potassium bromide (KBr) pellets and kept in a dry environment throughout the characterization process. The spectra were collected over the range of 500–4000 cm^{-1}, with each consisting of 64 scans at a resolution of 1 cm-1.

In situ liquid-state ^{1}H NMR spectra were acquired using a Varian 400 MHz NMR spectrometer at 25 ℃. BDC and Zn(OAc)$_2$ were pre-dissolved in DMF separately. A 300 μL volume of DMF-d_7 was transferred to the NMR tube, followed by the addition of the Zn(OAc)$_2$ solution and then the BDC solution. The final concentrations of Zn(OAc)$_2$ and BDC in the tube were 0.05 M and 0.025 M, respectively. For the reaction systems containing TOCNF, the TOCNF was pre-solvent exchanged with DMF, and the final concentration in the tube was 0.1 wt%. The mixture was immediately vortexed and inserted into the instrument to start signal acquisition within 2-3 minutes of adding BDC. We note that the *in situ* NMR measurements were conducted at 25 ℃ due to the temperature limitations of the NMR probe. Each spectrum was acquired over 2.5 minutes, with a 5-second delay before starting the next sequence. The spectra were processed and analyzed using Mnova software, with the DMF peak at δ_H of 2.92 ppm used as the reference for chemical shift calibration.

TOCNF model construction

The initial model of the Iβ cellulose crystal containing 36 glucose chains was obtained using the Cellulose Builder toolkit.[68] The model was then revised to an 18-chain configuration as recent scientific evidence indicates that the elementary microfibril in plants consists of 18 chains.[69-71] The modification was achieved by removing the outermost 18 chains from the original model, retaining the core 18 chains. Next, to build the TOCNF model,

the C6 primary hydroxyl groups located on every second glucosyl unit—those exposed on the cellulose crystal surfaces (outmost 12 chains)—were converted into carboxylates.[18] This is because TEMPO oxidation-induced carboxylation occurs on the surface of the cellulose fibril, instead of the internal core region.[65, 67] Previous studies have suggested that higher concentrations of carboxylates can weaken the noncovalent interchain interactions, thereby facilitating the disassembly of cellulose crystals.[72] In this study, we employed a relatively lower carboxylate concentration to prevent this issue. In our experiments, the prepared TOCNF exhibited a carboxylate concentration of 0.7 mmol/g. For simulation, we modified our TOCNF model by converting three C6 hydroxyl groups on each outer layer chain into carboxylates. This modification introduces a total of 36 carboxylates into the model, corresponding to a final carboxylate concentration of 0.61 mmol/g, which is in approximate agreement with the carboxylate content measured in the wet experiment.

The TOCNF model is illustrated in **Fig. S1**. This model comprises 18 glucose chains, each containing 20 glucose monomers, with 36 carboxylates present on the surface. The cellulose crystal exhibits a hexagonal cross-section, oriented along the (100), (110), and (1-10) crystallographic directions. The overall structure of TOCNF model has a dimension of 2.2 × 3.5 × 10.3 nm^3.

Simulation details

Classical all-atom molecular dynamics simulations were performed using the GROMACS 2021.5 package.[73] The simulation system contains Zn ions, BDC ligands, and TOCNF. Acetate was used as counterions, and DMF was used as the solvent. The force field parameters for the Zn ion dummy model were derived from earlier studies.[74, 75] The dummy model is characterized by an octahedral geometry, where the central Zn atom is encircled by six dummy atoms. Detailed parameters of the dummy model are provided in **Table S1**. The coordinates for TOCNF and the Zn dummy model are provided in the Supplementary information.

CHARMM36 force field was used for all other atoms.[76, 77] The leap-frog integrator was used with a time step of 2 fs. The cutoff for nonbonded interactions was set to 12 Å. The Particle Mesh Ewald (PME) method [78] was employed for long-range electrostatic interactions. The temperature was maintained at 393.15 K using a Berendsen thermostat [79] with a coupling constant of 0.1 ps. The LINCS algorithm [80] was utilized for bond constraints involving hydrogen atoms. The Parrinello-Rahman barostat [81] was used with a time constant of 2 ps to maintain a pressure of 1 bar. The simulation system was subjected to energy minimization followed by 0.1 ns of NVT and 0.1 ns of NPT equilibration before the final production run.

We conducted one simulation, designated as S$_{MOF}$, to focus on the assembly of Zn and BDC for pristine MOF. Another five simulations, designated as S$_{Hybrid-1}$ to S$_{Hybrid-5}$, were performed with varying contents of Zn ions, BDC, and acetates to examine the assembly of Zn and BDC on TOCNF. For these S$_{Hybrid}$ simulations, three replicates were performed by initializing random velocities prior to equilibration and final production.

Additionally, a smaller simulation box, designated as $S_{MOF\text{-small}}$ and containing a reduced number of MOF precursors, was run for an extended time of 500 ns to ensure convergence. A detailed summary of the simulations is provided in **Table S2**.

The MD trajectory analysis was conducted using GROMACS and in-house Python code built based on the MDAnalysis package.[82] Visualization of molecular configurations from the simulation trajectories was performed using VMD software.[83]

Conflicts of interest

There are no conflicts to declare.

Data availability

The authors confirm that the data supporting the findings of this study are available within the article [and/or] its ESI. Additional data will be made available on request.

Acknowledgments

Notes and references

1.   H. Furukawa, K. E. Cordova, M. O'Keeffe and O. M. Yaghi, *Science*, 2013, **341**, 1230444.
2.   S. Kitagawa, *Chem. Soc. Rev.*, 2014, **43**, 5415-5418.
3.   L. Jiao, J. Y. R. Seow, W. S. Skinner, Z. U. Wang and H.-L. Jiang, *Mater. Today*, 2019, **27**, 43-68.
4.   S. Rojas and P. Horcajada, *Chem. Rev.*, 2020, **120**, 8378-8415.
5.   X. Luan, Z. Xiang, J. Dong, C. Wang, X. Li, Q. Shi and X. Du, *ACS Appl. Mater. Interfaces*, 2023, **15**, 27264-27276.
6.   Y. Liu, X. Li, S. Zhang, Z. Wang, Q. Wang, Y. He, W. H. Huang, Q. Sun, X. Zhong and J. Hu, *Adv. Mater.*, 2023, **35**, 2300945.
7.   C. Hong, L. Li, J. Y. Zou, L. Zhang and S. Y. You, *Dalton Trans.*, 2023, **52**, 6067-6076.
8.   X. X. Wang, D. H. Guan, C. L. Miao, D. C. Kong, L. J. Zheng and J. J. Xu, *J. Am. Chem. Soc.*, 2023, **145**, 5718-5729.
9.   Z. Zhu, H. Tsai, S. T. Parker, J.-H. Lee, Y. Yabuuchi, H. Z. Jiang, Y. Wang, S. Xiong, A. C. Forse and B. Dinakar, *J. Am. Chem. Soc.*, 2024, **146**, 6072-6083.
10.   K. Dassouki, S. Dasgupta, E. Dumas and N. Steunou, *Chem. Sci.*, 2023, **14**, 12898-12925.
11.   B. Deeraj, J. S. Jayan, A. Raman, A. Asok, R. Paul, A. Saritha and K. Joseph, *Surf. Interfaces*, 2023, **43**, 103574.
12.   W. L. Teo, W. Zhou, C. Qian and Y. Zhao, *Mater. Today*, 2021, **47**, 170-186.
13.   G. W. Peterson, D. T. Lee, H. F. Barton, T. H. Epps III and G. N. Parsons, *Nat. Rev. Mater.*, 2021, **6**, 605-621.
14.   H. N. Abdelhamid and A. P. Mathew, *Coord. Chem. Rev.*, 2022, **451**, 214263.
15.   T. Li, C. Chen, A. H. Brozena, J. Zhu, L. Xu, C. Driemeier, J. Dai, O. J. Rojas, A. Isogai and L. Wågberg, *Nature*, 2021, **590**, 47-56.
16.   T. Devic and C. Serre, *Chem. Soc. Rev.*, 2014, **43**, 6097-6115.
17.   L. Feng, K. Y. Wang, J. Willman and H. C. Zhou, *ACS Cent. Sci.*, 2020, **6**, 359-367.
18.   A. Isogai, T. Saito and H. Fukuzumi, *Nanoscale*, 2011, **3**, 71-85.
19.   Q. Li and S. Renneckar, *Biomacromolecules*, 2011, **12**, 650-659.
20.   L. Zhu, L. Zong, X. Wu, M. Li, H. Wang, J. You and C. Li, *ACS Nano*, 2018, **12**, 4462-4468.
21.   Z. Yuan, D. Meng, Y. Wu, G. Tang, P. Liang, J. H. Xin and D. Ye, *Nano Res.*, 2022, **15**, 2599–2607.
22.   M. L. Kim, E. H. Otal and J. P. Hinestroza, *Cellulose*, 2019, **26**, 123-137.
23.   S. Zhou, M. Stromme and C. Xu, *Chem. - Eur. J.*, 2019, **25**, 3515-3520.
24.   F. Tan, L. Zha and Q. Zhou, *Adv. Mater.*, 2022, **34**, e2201470.
25.   J. Qiao, Q. Song, X. Zhang, S. Zhao, J. Liu, G. Nystrom and Z. Zeng, *Adv. Sci. (Weinheim, Ger.)*, 2024, **11**, 2400403.
26.   M. Li, Y. Mu, Q. Xu, L. Jin and Y. Fu, *Ind. Crops Prod.*, 2024, **208**, 117876.
27.   R. Goeminne, L. Vanduyfhuys, V. Van Speybroeck and T. Verstraelen, *J. Chem. Theory Comput.*, 2023, **19**, 6313-6325.
28.   M. Islamov, H. Babaei, R. Anderson, K. B. Sezginel, J. R. Long, A. J. McGaughey, D. A. Gomez-Gualdron and C. E. Wilmer, *npj Comput. Mater.*, 2023, **9**, 11.
29.   R. Xin, C. Wang, Y. Zhang, R. Peng, R. Li, J. Wang, Y. Mao, X. Zhu, W. Zhu, M. Kim, H. N. Nam and Y. Yamauchi, *ACS Nano*, 2024, **18**, 19403-19422.
30.   T. K. Piskorz, V. Marti-Centelles, T. A. Young, P. J. Lusby and F. Duarte, *ACS Catal.*, 2022, **12**, 5806-5826.
31.   M. Yoneya, T. Yamaguchi, S. Sato and M. Fujita, *J. Am. Chem. Soc.*, 2012, **134**, 14401-14407.
32.   M. Yoneya, S. Tsuzuki, T. Yamaguchi, S. Sato and M. Fujita, *ACS Nano*, 2014, **8**, 1290-1296.
33.   M. Yoneya, S. Tsuzuki and M. Aoyagi, *Phys. Chem. Chem. Phys.*, 2015, **17**, 8649-8652.
34.   D. Biswal and P. G. Kusalik, *ACS Nano*, 2017, **11**, 258-268.
35.   Y. J. Colon, A. Z. Guo, L. W. Antony, K. Q. Hoffmann and J. J. de Pablo, *J. Chem. Phys.*, 2019, **150**, 104502.
36.   T. A. Maula, H. W. Hatch, V. K. Shen, S. Rangarajan and J. Mittal, *Mol. Syst. Des. Eng.*, 2019, **4**, 644-653.
37.   S. A. Wells, N. F. Cessford, N. A. Seaton and T. Duren, *RSC Adv.*, 2019, **9**, 14382-14390.
38.   S. R. G. Balestra and R. Semino, *J. Chem. Phys.*, 2022, **157**, 184502.
39.   L. Kollias, R. Rousseau, V. A. Glezakou and M. Salvalaglio, *J. Am. Chem. Soc.*, 2022, **144**, 11099-11109.
40.   B. B. Skjelstad, Y. Hijikata and S. Maeda, *Inorg. Chem.*, 2023, **62**, 1210-1217.

41.   J. Yang, F. Xu and C.-R. Han, *Biomacromolecules*, 2017, **18**, 1019-1028.

42.   M. Chau, S. E. Sriskandha, D. Pichugin, H. Therien-Aubin, D. Nykypanchuk, G. Chauve, M. Methot, J. Bouchard, O. Gang and E. Kumacheva, *Biomacromolecules*, 2015, **16**, 2455-2462.

43.   J.-M. Yang, Q. Liu and W.-Y. Sun, *Microporous Mesoporous Mater.*, 2014, **190**, 26-31.

44.   H. Li, M. Eddaoudi, T. L. Groy and O. Yaghi, *J. Am. Chem. Soc.*, 1998, **120**, 8571-8572.

45.   M. Edgar, R. Mitchell, A. M. Slawin, P. Lightfoot and P. A. Wright, *Chem. - Eur. J.*, 2001, **7**, 5168-5175.

46.   M. S. Biserčić, B. Marjanović, B. N. Vasiljević, S. Mentus, B. A. Zasońska and G. Ćirić-Marjanović, *Microporous Mesoporous Mater.*, 2019, **278**, 23-29.

47.   L. Zhang and Y. H. Hu, *Mater. Sci. Eng., B*, 2011, **176**, 573-578.

48.   J. Xing, L. Schweighauser, S. Okada, K. Harano and E. Nakamura, *Nat. Commun.*, 2019, **10**, 3608.

49.   C. K. Brozek, V. K. Michaelis, T. C. Ong, L. Bellarosa, N. Lopez, R. G. Griffin and M. Dinca, *ACS Cent. Sci.*, 2015, **1**, 252-260.

50.   C. J. Tatebe, S. Yusuf, M. K. Bellas, M. Zeller, C. Arntsen and D. T. Genna, *Cryst. Growth Des.*, 2021, **21**, 6840-6846.

51.   N. Gimeno and R. Vilar, *Coord. Chem. Rev.*, 2006, **250**, 3161-3189.

52.   K. Gura, J. L. Hirst and C. Mummert, *Computability*, 2015, **4**, 103-117.

53.   R. Van Santen, *J. Phys. Chem.*, 1984, **88**, 5768-5769.

54.   G. K. Kole and J. J. Vittal, *Chem. Soc. Rev.*, 2013, **42**, 1755-1775.

55.   M. J. Van Vleet, T. Weng, X. Li and J. R. Schmidt, *Chem. Rev.*, 2018, **118**, 3681-3721.

56.   A. G. Hawkes, *Quantitative Finance*, 2018, **18**, 193-198.

57.   P. J. Laub, T. Taimre and P. K. Pollett, *arXiv preprint arXiv:1507.02822*, 2015.

58.   E. N. Brown, R. Barbieri, V. Ventura, R. E. Kass and L. M. Frank, *Neural Computation*, 2002, **14**, 325-346.

59.   R. M. Abdelhameed, H. E. Emam, J. Rocha and A. M. Silva, *Fuel Process. Technol.*, 2017, **159**, 306-312.

60.   J. J. De Yoreo, P. U. Gilbert, N. A. Sommerdijk, R. L. Penn, S. Whitelam, D. Joester, H. Zhang, J. D. Rimer, A. Navrotsky, J. F. Banfield, A. F. Wallace, F. M. Michel, F. C. Meldrum, H. Colfen and P. M. Dove, *Science*, 2015, **349**, aaa6760.

61.   B. P. Carpenter, A. R. Talosig, B. Rose, G. Di Palma and J. P. Patterson, *Chem. Soc. Rev.*, 2023, **52**, 6918-6937.

62.   B. J. Burnett and W. Choe, *Dalton Trans.*, 2012, **41**, 3889-3894.

63.   C. N. Rao, S. Natarajan, A. Choudhury, S. Neeraj and A. A. Ayi, *Acc. Chem. Res.*, 2001, **34**, 80-87.

64.   C. R. Marshall, S. A. Staudhammer and C. K. Brozek, *Chem. Sci.*, 2019, **10**, 9396-9408.

65.   T. Saito, S. Kimura, Y. Nishiyama and A. Isogai, *Biomacromolecules*, 2007, **8**, 2485-2491.

66.   K. Zhang, T. Elder, Z. Cheng, K. Zhan, Y. Peng and M. Li, *J. Environ. Chem. Eng.*, 2024, **12**, 112670.

67.   T. Saito and A. Isogai, *Biomacromolecules*, 2004, **5**, 1983-1989.

68.   T. C. Gomes and M. S. Skaf, *J. Comput. Chem.*, 2012, **33**, 1338-1346.

69.   J. L. Hill, Jr., M. B. Hammudi and M. Tien, *The Plant Cell*, 2014, **26**, 4834-4842.

70.   B. T. Nixon, K. Mansouri, A. Singh, J. Du, J. K. Davis, J. G. Lee, E. Slabaugh, V. G. Vandavasi, H. O'Neill, E. M. Roberts, A. W. Roberts, Y. G. Yingling and C. H. Haigler, *Sci. Rep.*, 2016, **6**, 28696.

71.   J. D. Kubicki, H. Yang, D. Sawada, H. O'Neill, D. Oehme and D. Cosgrove, *Sci. Rep.*, 2018, **8**, 13983.

72.   G. H. Silvestre, L. O. Pinto, J. S. Bernardes, R. H. Miwa and A. Fazzio, *J. Phys. Chem. B*, 2021, **125**, 3717-3724.

73.   M. J. Abraham, T. Murtola, R. Schulz, S. Páll, J. C. Smith, B. Hess and E. Lindahl, *SoftwareX*, 2015, **1**, 19-25.

74.   F. Duarte, P. Bauer, A. Barrozo, B. A. Amrein, M. Purg, J. Aqvist and S. C. Kamerlin, *J. Phys. Chem. B*, 2014, **118**, 4351-4362.

75.   Q. Liao, S. C. L. Kamerlin and B. Strodel, *J. Phys. Chem. Lett.*, 2015, **6**, 2657-2662.

76.   J. Huang and A. D. MacKerell, Jr., *J. Comput. Chem.*, 2013, **34**, 2135-2145.

77.   K. Vanommeslaeghe and A. D. MacKerell, Jr., *J. Chem. Inf. Model.*, 2012, **52**, 3144-3154.

78.   D. M. York, T. A. Darden and L. G. Pedersen, *J. Chem. Phys.*, 1993, **99**, 8345-8348.

79.   H. J. Berendsen, J. v. Postma, W. F. Van Gunsteren, A. DiNola and J. R. Haak, *J. Chem. Phys.*, 1984, **81**, 3684-3690.

80.   B. Hess, H. Bekker, H. J. Berendsen and J. G. Fraaije, *J. Comput. Chem.*, 1997, **18**, 1463-1472.

81.   M. Parrinello and A. Rahman, *J. Appl. Phys.*, 1981, **52**, 7182-7190.

82.   N. Michaud-Agrawal, E. J. Denning, T. B. Woolf and O. Beckstein, *J. Comput. Chem.*, 2011, **32**, 2319-2327.

83.   W. Humphrey, A. Dalke and K. Schulten, *J. Mol. Graphics*, 1996, **14**, 33-38, 27-38.

Data availability

The authors confirm that the data supporting the findings of this study are available within the article [and/or] its ESI. Additional data will be made available on request.